© 2018. Published by The Company of Biologists Ltd | Journal of Cell Science (2018) 131, jcs223107. doi:10.1242/jcs.223107

RESEARCH ARTICLE

Local microtubule organization promotes cargo transport in *C. elegans* dendrites

Martin Harterink[1,*], Stacey L. Edwards[2], Bart de Haan[1], Kah Wai Yau[1], Sander van den Heuvel[3], Lukas C. Kapitein[1], Kenneth G. Miller[2] and Casper C. Hoogenraad[1,*]

ABSTRACT

The specific organization of the neuronal microtubule cytoskeleton in axons and dendrites is an evolutionarily conserved determinant of neuronal polarity that allows for selective cargo sorting. However, how dendritic microtubules are organized and whether local differences influence cargo transport remains largely unknown. Here, we use live-cell imaging to systematically probe the microtubule organization in *Caenorhabditis elegans* neurons, and demonstrate the contribution of distinct mechanisms in the organization of dendritic microtubules. We found that most non-ciliated neurons depend on *unc-116* (kinesin-1), *unc-33* (CRMP) and *unc-44* (ankyrin) for correct microtubule organization and polarized cargo transport, as previously reported. Ciliated neurons and the URX neuron, however, use an additional pathway to nucleate microtubules at the tip of the dendrite, from the base of the cilium in ciliated neurons. Since inhibition of distal microtubule nucleation affects distal dendritic transport, we propose a model in which the presence of a microtubule-organizing center at the dendrite tip ensures correct dendritic cargo transport.

KEY WORDS: *C. elegans*, MTOC, Dendrite, Microtubule, Polarity

INTRODUCTION

Neurons use axons and dendrites to communicate with other cells in the nervous system. The microtubule cytoskeleton is of critical importance to functionally differentiate these two compartments. Microtubules are polymers of α- and β-tubulin, and have an intrinsic polarity, which is exploited by microtubule motors to transport cargo in a directional manner. Whereas axonal microtubules are organized with their plus-ends pointing outwards, dendrites have either a mixed or a uniform 'minus-end out' microtubule organization (Baas and Lin, 2011). This polarized microtubule organization in neurons allows for axonal targeting by motors of the plus-end-directed kinesin family, and suggests a more prominent role for the minus-end-directed motor, dynein, to target the dendrite (Kapitein and Hoogenraad, 2015; Rolls and Jegla, 2015). In addition, microtubule length, stability and dynamics have also been shown to be important for the regulation of transport in axons and dendrites (Kurup et al., 2015; Tas et al., 2017; Yogev et al., 2016, 2017). How axon and dendrite microtubule organizations are established remains largely unknown.

It is thought that a combination of local microtubule nucleation (Kurup et al., 2015; Tas et al., 2017; Yogev et al., 2016, 2017) with microtubule sliding and stabilization (del Castillo et al., 2015; Rao et al., 2017; Sanchez-Huertas et al., 2016; van Beuningen et al., 2015; Zheng et al., 2008) is responsible for the organization of the neuronal microtubule network. The centrosome, which in dividing cells is largely responsible for organizing the microtubules, in neurons is considered to lose its function as a microtubule-organizing center (MTOC) during maturation (Stiess et al., 2010). However, in electron microscopy studies, microtubules have been found to anchor to the base of the sensory cilium (basal body) located at the tip of dendrites in olfactory neurons and photoreceptor cells (Burton, 1985; Reese, 1965; Troutt et al., 1990). Since the cilium is nucleated by the centriole, normally located at the heart of the centrosome, this may suggest that, in these neurons, the basal body still functions as a MTOC and thus raises the question of whether the presence of a distal cilium affects neuronal microtubule organization. Since the relative contribution of such mechanisms is expected to vary between neuron types, there is a need to systematically analyze neuronal microtubule organization.

In this study, we used live-cell imaging to systematically probe neuronal microtubule organization in the nematode *Caenorhabditis elegans*. Using this model, we were able to analyze diverse neuron types *in vivo* with high reproducibility since the cell lineage is invariant. We also analyzed previously described mutants with neuronal microtubule organization defects (Goodwin et al., 2012; Maniar et al., 2011; Yan et al., 2013), and found substantial neuron-specific requirements for these genes. While some neurons are largely dependent on these genes to organize dendritic microtubules, ciliated neurons and the URX neuron additionally have an MTOC at the dendrite tip, which promotes distal cargo transport.

RESULTS

C. elegans axons and dendrites have parallel microtubules of opposite polarity

To analyze microtubule organization in *C. elegans* neurons, we expressed the microtubule plus-tip marker EBP-2::GFP under the control of neuron-specific promoters. The EBP-2 marker only localizes to the microtubule plus-end during phases of microtubule growth, and thus can be used to infer microtubule polarity (Fig. 1A) (Stepanova et al., 2003). For the analysis, we selected eight different neurons that possess more than one neurite; six sensory neurons, one motor neuron and the bipolar CAN neuron. Although pre- and post-synaptic domains are not always restricted to one neurite (such as for the PLM neuron; Bounoutas and Chalfie, 2007), we tentatively assigned each neurite as an axon or dendrite. For some neurites, dendrite identity is obvious due to a distal sensory cilium,

[1]Cell Biology, Department of Biology, Faculty of Science, Utrecht University, Padualaan 8, 3584 Utrecht, The Netherlands. [2]Genetic Models of Disease Program, Oklahoma Medical Research Foundation, Oklahoma City, OK 73104, US. [3]Developmental Biology, Department of Biology, Faculty of Science, Utrecht University, Padualaan 8, 3584 Utrecht, The Netherlands.

*Authors for correspondence (m.harterink@uu.nl; c.hoogenraad@uu.nl)

M.H., 0000-0002-8256-6651; K.W.Y., 0000-0003-1504-3604; S.v.d.H., 0000-0001-9015-7463; L.C.K., 0000-0001-9418-6739; C.C.H., 0000-0002-2666-0758

Received 23 July 2018; Accepted 14 September 2018

Journal of Cell Science (2018) 131, jcs223107. doi:10.1242/jcs.223107

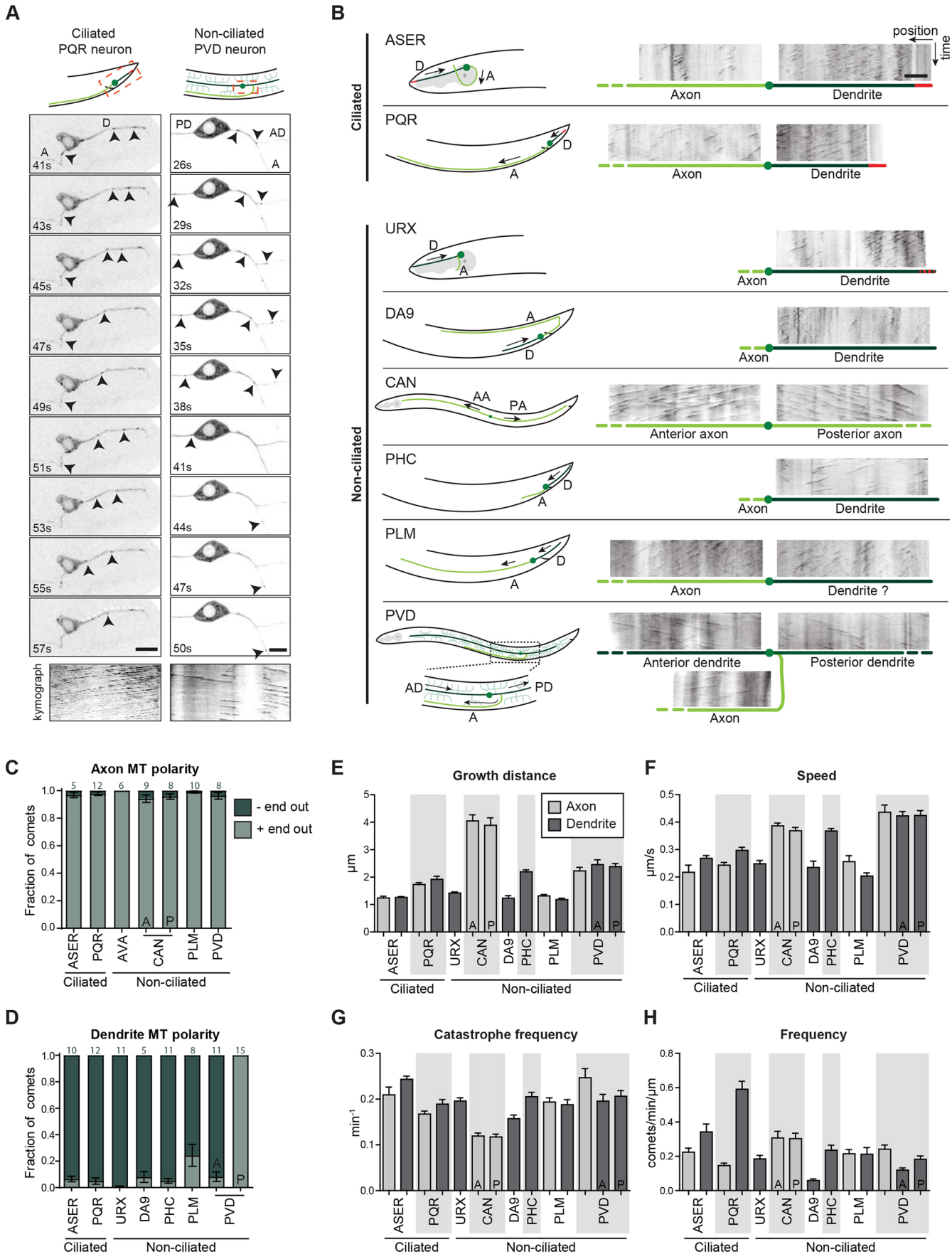

Fig. 1. See next page for legend.

Journal of Cell Science

Journal of Cell Science (2018) 131, jcs223107. doi:10.1242/jcs.223107

Fig. 1. Systematic analyses of microtubule dynamics in *C. elegans* neurons. (A,B) Neuron-specific expression of the microtubule plus-end marker EBP-2::GFP, which is a homolog of human EB1–EB3 (also known as MAPRE1–MAPRE3). (A) Representative stills of EBP-2::GFP dynamics (marked by arrowheads) in the PQR and PVD neuron and the corresponding kymograph (time, vertically, of 120 s) from Movies 1 and 2. (B) Overview of the analyzed neurons in this paper and example kymographs to illustrate the microtubule polarity. The PLM posterior neurite was grouped with the dendrites based on its microtubule polarity. Movies/kymographs were taken at 1 fps for 120 s. A, axon (light green); D, dendrite (dark green); AD, anterior dendrite; PD, posterior dendrite; AA, anterior axon; PA, posterior axon; cilia, red. Scale bars: 5 µm. (C–H) Quantification of the proportion of microtubules showing the indicated polarity (C,D) and EBP-2 dynamics (E–H) in ≥10 animals (or 5 for the AVA neuron). For C,D, only neurites from animals with ≥10 EBP-2 growth events were used (number of animals is indicated at the top of the bars). For the CAN and PVD neurons, A is anterior and P is posterior. Error bars are s.e.m.

which we separately depict in Fig. 1. The cilium is formed by a centriole-derived basal body, which in *C. elegans* degenerate after forming the cilium (Li et al., 2017; Nechipurenko et al., 2017; Serwas et al., 2017). Live imaging of EBP-2::GFP was performed along the length of each neurite in at least ten animals. The axons of URX, DA9 and PCH were not analyzed due to overlapping neurons or complicated morphology. For each movie, we made a kymograph to represent the microtubule dynamics, which we used to quantify microtubule polarity and plus-tip parameters (Fig. 1A,B; Movies 1,2). As expected, in all seven axons analyzed, the plus-tip marker moves away from the cell body showing that the microtubules are organized in a parallel plus-end out manner (Fig. 1B,C), as reported for other organisms (Kapitein and Hoogenraad, 2015). This includes both neurites from the symmetric CAN neuron, which has been described to possess two axons (Modzelewska et al., 2013). In dendrites, however, microtubules have a nearly complete minus-end out organization in both ciliated as well as non-ciliated neurons (Fig. 1B,D). Some dendrites have a small portion of plus-end out microtubules, which are mainly seen close to the cell body and not in the distal dendrite (Fig. S2C). This suggests that microtubules occasionally grow from the cell body into the dendrite but do not get stabilized. There is, however, one clear exception; the primary branch of the PVD anterior dendrite has uniform minus-end out microtubules, while the structurally identical posterior branch has plus-end out microtubules (Fig. 1D) (Taylor et al., 2015). Since the PVD axon and posterior dendrite have the same microtubule polarity organization, additional regulatory mechanisms are likely to mediate selective cargo delivery into each neurite. The side branches of the PVD dendrites are largely devoid of microtubules (Fig. S1A; Maniar et al., 2011), but we occasionally observed dynamic microtubules without a preferred polarity (we observed 19 plus-end out and 11 minus-end out growth events in the side branches of the posterior dendrite).

When using a plus-tip marker to infer microtubule polarity, there is the danger of missing non-dynamic microtubules or of underrepresenting a population of longer microtubules as was the case for dendrites of rat hippocampal neurons (Baas et al., 1988; Burton, 1985; Stepanova et al., 2003). A laser-based microsurgery approach can be used to sever microtubules in a non-dynamic bundle, generating new plus-ends, which can be visualized with a plus-tip marker (Fig. 2A–F; Yau et al., 2016). By using this approach in *C. elegans* neurons, we found that laser severing caused a trend (although not significant) towards increased growth events around the cut site (Fig. 2G,I). Quantification of proportion of microtubule of each polarity, was in line with the observations made with EBP-2::GFP for both the axons, as well as for the dendrites of the ciliated PQR and non-ciliated PVD neurons (Fig. 2H,J), showing that, in all neurites, dynamic and non-dynamic microtubules have a parallel organization. Taken together, these data show that all *C. elegans* neurons analyzed have a plus-end out microtubule organization in axons and, in most cases, a minus-end out organization in dendrites in both ciliated and non-ciliated neurons, which confirms previous data (Goodwin et al., 2012; Maniar et al., 2011; Taylor et al., 2015; Yan et al., 2013).

Ciliated neurons and URX have an MTOC at the dendrite tip

In addition to analyzing microtubule polarity, the EBP-2::GFP data from various neuronal cell types allows us to study other characteristics of microtubule dynamics, including persistence, growth speed and catastrophe frequency. Overall, we observed pronounced differences between the neuronal subtypes (Fig. 1E–G). However, within each neuronal cell, the different microtubule parameters were very similar between the axon and dendrites. When we analyzed microtubule dynamics along single neurites in more detail, we found a marked decrease in microtubule growth events in the distal axonal region compared to the proximal region, suggesting that fewer and/or less-dynamic microtubules fill the distal axon (Fig. 3A). A similar pattern was observed for dendrites in most non-ciliated neurons (Fig. 3B). In contrast, ciliated dendrites show a substantially higher number of microtubule growth events in the distal segment, in particular close to the cilium (Fig. 3B,C; Movie 3). This also applies to the non-ciliated URX neuron (Figs 1B and 3B), which morphologically looks very similar to the other ciliated head neurons. Moreover, it has a specialized flattened sensory structure at the dendrite tip (Doroquez et al., 2014) and interestingly it expresses the cilia-specific gene *osm-6* (Fig. S1B).

To address whether these distal growth events are caused by local microtubule nucleation in dendrites, we analyzed the distribution of the microtubule nucleator γ-tubulin TBG-1. In non-ciliated neurons, γ-tubulin is diffusely localized throughout the neuron and is only slightly enriched at the dendrite tip (Fig. S3A). Ciliated neurons and URX show a consistent enrichment of γ-tubulin at the base of the cilium (Fig. S3A), as has been reported previously (Bobinnec et al., 2000). In line with these results, endogenously tagged GIP-2 (an essential subunit of the *C. elegans* γ-tubulin complex; Wang et al., 2015) accumulates at the tip of the dendrite in ciliated neurons but not in the non-ciliated PHC neuron (Fig. 3D–F). These data suggest that ciliated dendrites and URX have a distal MTOC that regulates microtubule nucleation.

C. elegans employs distinct mechanisms for minus-end out organization of dendritic microtubules

Since both dendrites with and without a distal MTOC have minus-end out microtubules, we wanted to address the relative contribution of the distal MTOC compared to that of previously described genes that have been found important for neuronal microtubule organization in *C. elegans*. Mutants for *cdk-5* (CDK5), *unc-33* (CRMP) and *unc-44* (ankyrin) were found to have mixed microtubule polarity in dendrites (Goodwin et al., 2012; Maniar et al., 2011), and in *unc-116* (kinesin-1) mutants the dendritic microtubules are switched into an axonal plus-end out organization (Yan et al., 2013). However, it is unclear whether these differences are caused by the presence or absence of a distal MTOC, since *unc-33* and *unc-44* were previously studied in ciliated neurons and *cdk-5* and *unc-116* in non-ciliated neurons. Therefore, we systematically analyzed these mutants in neurons with, as well as without, distal microtubule nucleation.

We found that the *unc-44* (ankyrin) mutation and to a lesser extent also *unc-33* (CRMP), affect neuronal development and lead

Journal of Cell Science (2018) 131, jcs223107. doi:10.1242/jcs.223107

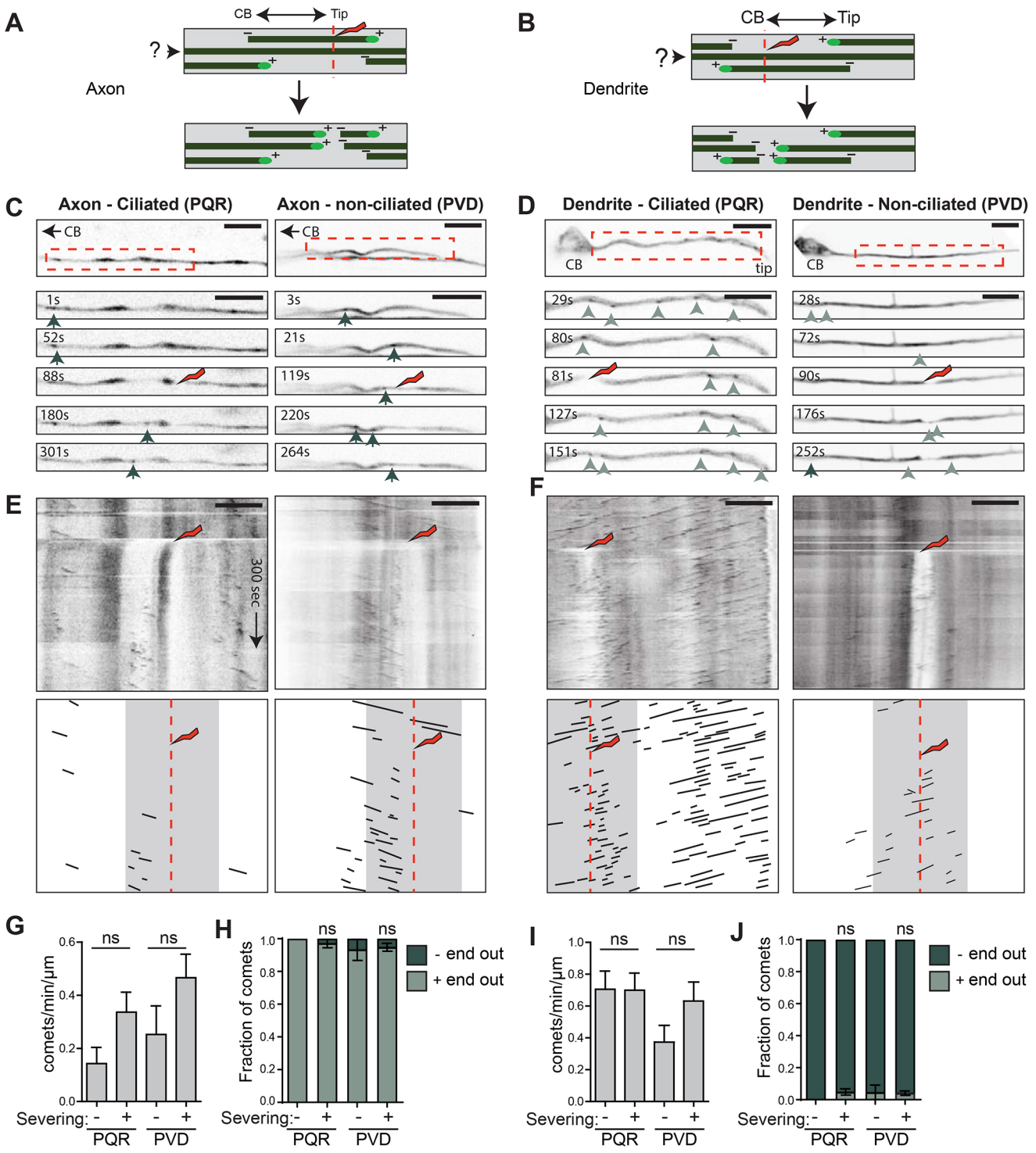

Fig. 2. Microtubule-severing experiments confirms uniform microtubule polarity in axons and dendrites. (A,B) Schematic representation of laser-induced microtubule-severing (red dotted line) experiments that generate new microtubule plus-tips that can be visualized using the EBP-2::GFP plus-tip marker in axons (A) or dendrites (B). (C,D) Stills of EBP-2::GFP imaging in the boxed area before and after laser-based severing in axon (C) and dendrites (D) of the ciliated PQR and non-ciliated PVD neuron. Dark green arrows point to EBP-2 moving away from the cell body (plus-end out microtubule), and light green arrowheads to EBP-2::GFP moving towards the cell body (minus-end out microtubule). Scale bars: 5 µm. (E,F) Kymographs of the stills in C and D with the schematic representation of the EBP-2 dynamics below. Note that after severing, there is an increase in EBP-2 dynamics proximal to the cut site in the axon (E) and to distal side for the dendrite (F), suggesting a short phase of microtubule depolymerization before growth. Scale bars: 5 µm. (G–J) Quantification of microtubule dynamics and polarity before and after cutting ($n \geq 5$ for axons and $n \geq 10$ for dendrites). ns, non-significant (Student's *t*-test); for H and J, microtubule polarity was compared to data from Fig. 1, since imaging time before cutting was limited. Error bars are s.e.m.

to severe microtubule defects in neurons without a distal MTOC (Fig. 4E-G). In the *unc-33* mutant, the dendritic microtubules in the PHC acquired a mixed organization, whereas in the PVD anterior dendrite this leads to a reversal in microtubule polarity (Fig. S2A,B), suggesting different *unc-33* requirements during neuron development. In dendrites with distal microtubule nucleation the contribution of the

Journal of Cell Science (2018) 131, jcs223107. doi:10.1242/jcs.223107

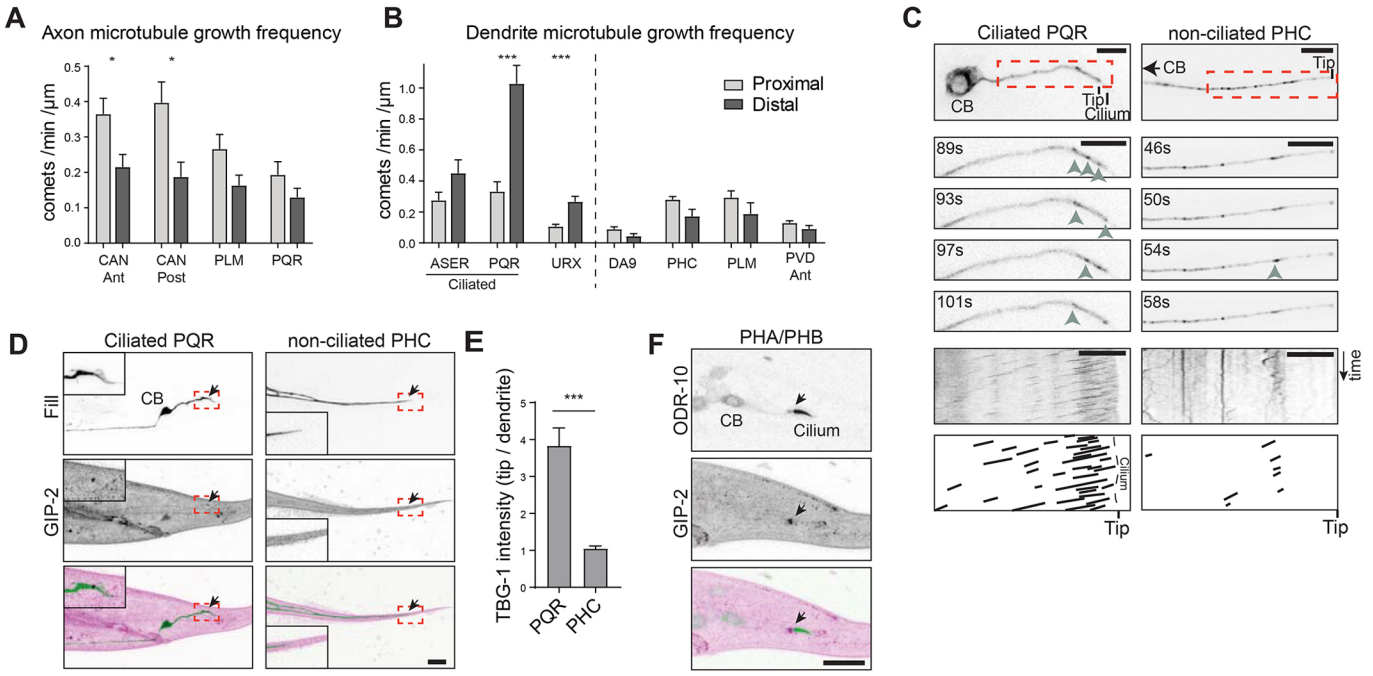

Fig. 3. Ciliated neurons and URX have an MTOC at the dendrite tip. (A) Quantification of EBP-2::GFP growth events in axons ($n \geq 10$). Proximal is defined as 0–20 µm and distal as >40 µm from the cell body. (B) Quantification of EBP-2::GFP growth events in ciliated and non-ciliated dendrites ($n \geq 10$). Proximal, proximal third of the dendrite; distal, distal third of the dendrite (except for the PVD anterior dendrite, which was quantified as for axons). (C) Example stills and kymographs of microtubule growth events (marked by arrowheads) at the tip of the dendrite from Movie 3. Kymographs show a time, vertically, of 120 s. Scale bars: 5 µm. (D) Endogenously tagged GIP-2::GFP accumulates at the tip of the ciliated PQR dendrite (arrow) but not the non-ciliated PHC dendrite tip. Fill, cytosolic mKate2. Magnifications of the highlighted areas are shown as insets. Scale bar: 10 µm. (E) Quantification of the amount of endogenously tagged GIP-2::GFP at the dendrite tip relative to that at the mid-dendrite ($n \geq 10$). (F) Endogenously tagged GIP-2::GFP accumulates at the base of the cilium (arrow) in the PHA/PHB neurons marked by cilium marker ODR-10. Scale bar: 10 µm. *P<0.05; ***P<0.005 (Student's t-test). Error bars are s.e.m. CB, cell body.

unc-33 and *unc-44* genes seems more limited (Fig. 4A–D; Fig. S2D,E). This is especially apparent for the URX dendrite, where the *unc-33* mutation does not affect microtubule polarity. For the ASER dendrite, some mixed microtubule polarity can be seen for both mutants, especially towards the cell body (Fig. S2D).

Similarly, when analyzing the commonly used partial-loss-of-function mutants for *unc-116* (kinesin-1), *e2310* and *r24s79*, we observed hardly any defects in neurons with distal microtubule nucleation and a partially penetrant microtubule polarity reversal phenotype in other neurons (Fig. 4A–D; Fig. S2). To test what occurs upon complete loss kinesin-1 function, we engineered Lox sites around the endogenous gene by using a novel approach to select for CRISPR/Cas9 genome editing events. As a marker for CRISPR editing events, we designed a *sup-1* minigene (only 1112 bps compared to 2129 bps for the commonly used *unc-119* marker) to suppress the uncoordinated phenotype of the *unc-17(e245)* mutant (see Materials and Methods; Fig. S4). To validate the floxed *unc-116(e815)* line, we assessed mitochondrial transport (Rawson et al., 2014) in *C. elegans* motor neurons and found that cell-specific expression of Cre markedly reduced the number of axonal mitochondria, especially in the proximal region where new mitochondria enter the axon (Fig. S4D,E). In the PVD neuron, depletion of *unc-116* via cell-specific Cre expression did not lead to obvious microtubule polarity defects, suggesting that enough *unc-116* mRNA and/or protein is present for correct neuronal development. However, expression of Cre before the birth of the PVD neuron led to a complete microtubule polarity reversal in the PVD anterior dendrite (Fig. 4E), suggesting that the partially penetrant phenotype seen in the *unc-116* mutants is due to the hypomorphic nature of the mutations. To also address the effect of full *unc-116* loss of function in ciliated neurons, we generated heterozygous null animals by excising *unc-116* in a heterozygous animal. Microtubule polarity was analyzed for the ASER dendrite in young homozygous larvae, since the null mutant is growth arrested. These animals had very similar defects to those observed for *unc-33* and *unc-44* loss of function (Fig. 4A). Finally, in mutants lacking *cdk-5*, we did not detect any defect in the neurons with or without distal microtubule nucleation (Fig. 4B,E), suggesting that the previously described effects of *cdk-5* mutations on dendritic microtubules is specific to DB motor neurons (Goodwin et al., 2012). Taken together, these data suggest that neurons without distal microtubule nucleation require *unc-116* (kinesin-1), *unc-33* (CRMP) and *unc-44* (ankyrin) to organize dendritic microtubules, while neurons with a distal MTOC are less dependent on these components (Fig. 5A).

To address whether polarized transport is differently affected by these mutants in neurons with or without distal microtubule nucleation, we analyzed the localization of the synaptic vesicles marked by RAB-3. In neurons with a distal MTOC (URX and PQR neurons), we did not see obvious RAB-3 mislocalization in *unc-33* and *unc-116* mutants, which is in agreement with these mutants having mild effects on dendritic microtubule organization. In a neuron lacking a distal MTOC (the PVD neuron), we observed considerable mislocalization of RAB-3 to the dendrites and/or cell body (Fig. S5).

Distal microtubule nucleation promotes cargo transport in the distal dendrite

To address how distal microtubule nucleation affects cargo transport, we analyzed the dendritic transport of secretory RAB-8 vesicles, which are thought to transport cargo to the cilium (Kaplan

Journal of Cell Science (2018) 131, jcs223107. doi:10.1242/jcs.223107

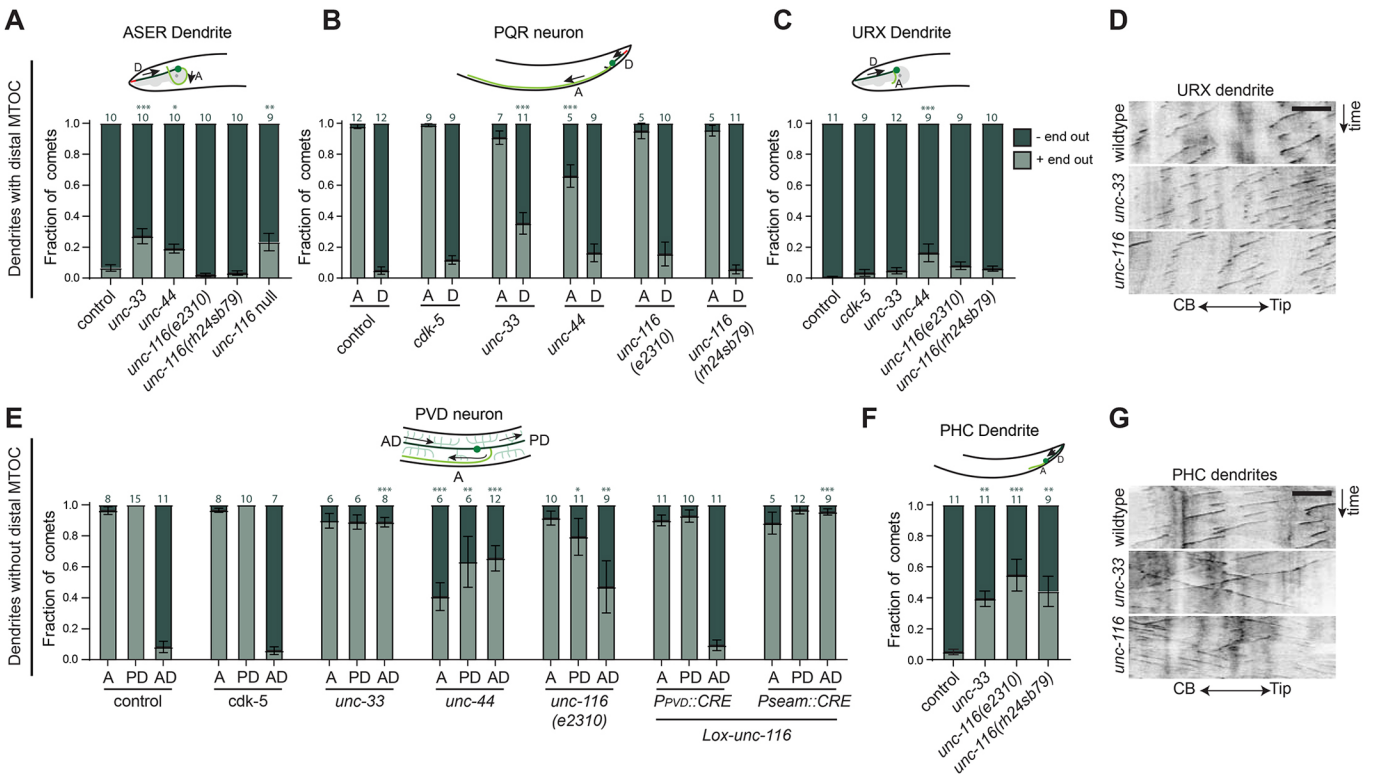

Fig. 4. Distinct mechanisms organize microtubules in the minus-end out configuration in dendrites. Quantification of microtubule polarity as determined with neuron-specific EBP-2::GFP expression in the *cdk-5(ok626)*, *unc-33(mn307)*, *unc-44(hrt2)* and indicated *unc-116* mutants. Additionally, for the PVD, results from a floxed *unc-116* allele with PVD-specific Cre expression (*Pdes-2*) or Cre expression in seam cells (skin) from which the PVD neuron is born (*Pwrt-2*) are shown. Only the neurites with ≥10 growth events were included in the analysis (*n* is indicated on top). Representative kymographs for the URX (D) and PHC (G) neurons are also shown. Kymographs are 120 s (vertically). Scale bar: 5 µm. A, axon (light green); D, dendrite (dark green); AD, anterior dendrite; PD, posterior dendrite. **P*<0.05; ***P*<0.01; ****P*<0.005 (one-way ANOVA followed by Dunnett's multiple comparisons test). Error bars are s.e.m. CB, cell body.

et al., 2010). We expressed GFP::RAB-8 in two neurons with and two neurons without distal microtubule nucleation, and compared the transport events in the proximal and distal dendrite. In dendrites with distal microtubule nucleation, RAB-8 is efficiently transported in both segments in a bidirectional manner (Fig. 5B,C). In dendrites without distal microtubule nucleation, however, RAB-8 is efficiently transported in the proximal segment but there is a significant decrease in transport events in the distal segment (Fig. 5B,C). To address whether distal microtubule nucleation is responsible for this difference in RAB-8 transport, we depleted the γ-tubulin complex subunit GIP-2 in a cell-specific manner. For this, we target the endogenously tagged GIP-2::GFP for proteasomal degradation using a fusion protein consisting of the anti-GFP-nanobody with ZIF-1, and expressing it using the *gcy-36* promoter, which is exclusively expressed in the PQR, URX and AQR neurons (Cheung et al., 2004). Since the protein depletion is initiated after initial neuron development, we did not see obvious developmental defects for the URX neuron and only occasional defects in PQR dendrite extension. We found that the GIP-2 depletion strategy led to a strong reduction of the GIP-2 signal at the tip of the PQR dendrite (Fig. S3B,C). Owing to surrounding basal bodies, the depletion of the GIP-2 protein could not be assessed for the URX; however, the knockdown strategy led to a marked loss in distal microtubule dynamics in this neuron (Fig. 5E). We did not observe changes in microtubule polarity, even in the *unc-33* and *unc-116* mutant backgrounds (Fig. S2F). This suggests that GIP-2 depletion is incomplete or acts too late to induce microtubule polarity defects, although we cannot exclude the possibility that additional mechanisms have a role in this process. When examining RAB-8 transport upon the same GIP-2 depletion approach, we observed a significant decrease in distal RAB-8 transport, whereas the proximal transport events remained unchanged (Fig. 5F). Similarly, upon GIP-2 depletion, we observed increased differences between proximal and distal transport of Golgi structures, labeled with an AMAN-2 fragment (mannosidase II; Fig. 5G). Finally, we also observed a marked reduction in GCY-35 (guanylyl cyclase) targeting to the distal sensory structure of the URX (Fig. 5H,I).

The presence of increased microtubule dynamics in the distal dendrite might promote transport to the tip, since microtubule plus-tips are suggested to facilitate dynein landing on the microtubule (Moughamian et al., 2013). To address whether microtubule dynamics in the distal segment are important for the efficient transport, we used the microtubule stabilizer Taxol to reduce the number of plus-tips without decreasing microtubule numbers. Incubation with Taxol did not lead to changes in RAB-8 transport in the ASER neuron, whereas it efficiently inhibited all plus-tip dynamics (Fig. 5J,K). This suggests that the presence of dendrite-tip-anchored microtubules, and not their dynamics, promotes distal cargo transport.

DISCUSSION

The differential organization of microtubule polarity between axons and dendrites is an evolutionarily conserved determinant of axon–dendrite polarity allowing for selective targeting of proteins and organelles to either neurite by means of specific microtubule motors. Although several mechanisms have been proposed to contribute to the establishment of dendritic minus-end out microtubules, their relative contributions are still largely unclear.

Journal of Cell Science (2018) 131, jcs223107. doi:10.1242/jcs.223107

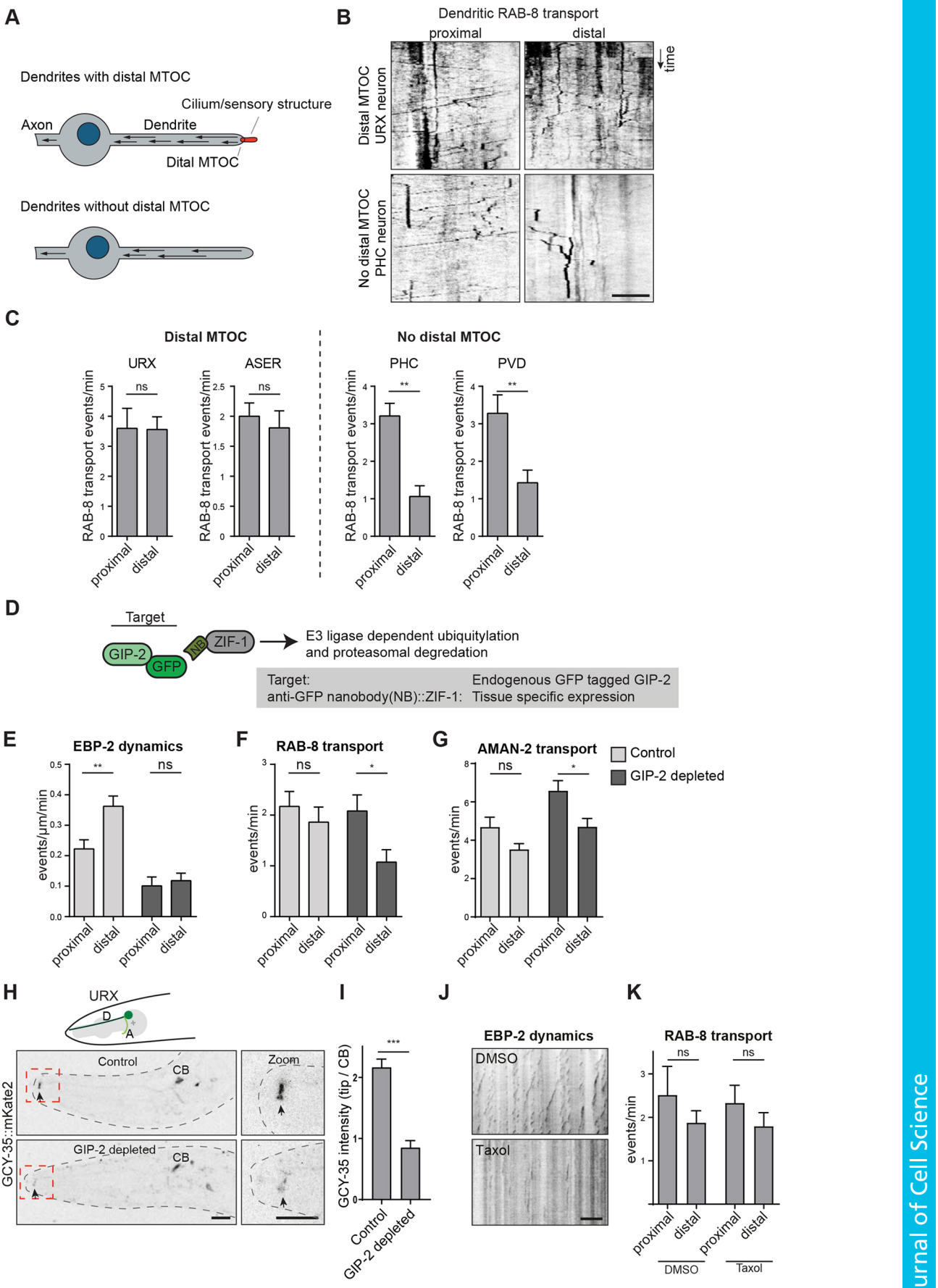

Fig. 5. See next page for legend.

Fig. 5. Distal dendritic microtubule nucleation promotes RAB-8 transport. (A) Model. Ciliated neurons and URX have strong microtubule nucleation from the dendrite tip. Dynamic microtubules are represented as arrows, indicating the intrinsic polarity pointing to the plus-tip. (B) Representative kymographs of dendritic RAB-8 transport in the proximal and distal dendrite of the URX and PHC neurons. All images are oriented with the cell body (CB) to the left and the tip to the right. Time, 120 s (vertically). Scale bar: 5 µm. (C) Quantification of RAB-8 transport in URX (n=5), ASER (n=12), PHC (n=5) and PVD (n=10) neurons. (D) Schematic mechanism of cell-specific inhibition of microtubule nucleation as developed by the Oegema labortory (Wang et al., 2015). The γ-tubulin complex subunit GIP-2 is endogenously tagged with GFP, which can be targeted for degradation through cell-specific expression of a fusion protein consisting of the anti-GFP nanobody and ZIF-1. (E–G) Quantification of microtubule dynamics (E) as well as RAB-8 (F) and AMAN-2 (G) transport in worms with URX-specific GIP-2 depletion (n≥10). (H,I) Representative images and quantification of cilium targeting of GCY-35 in the URX neuron upon URX-specific GIP-2 depletion (n=11). Scale bar: 10 µm. (J,K) Representative kymographs of microtubule dynamics in the URX dendrite upon Taxol incubation [kymograph, 2 min (vertically)], and quantification of proximal and distal RAB-8 transport upon Taxol incubation. Scale bar: 5 µm. *P<0.05; **P<0.01; ***P<0.005; ns, not significant (Student's t-test,). Error bars are s.e.m.

Moreover, these studies have looked at various neurons and model systems making it hard to compare and interpret these data. In this study, we have systematically analyzed microtubule organization in *C. elegans* neurons.

Local microtubule organization facilitates cargo transport

We found that *C. elegans* employs distinct mechanisms to organize dendritic microtubules with a minus-end out polarity; non-ciliated neurons require *unc-116* (kinesin-1), *unc-33* (CRMP) and *unc-44* (ankyrin), while ciliated neurons, including URX, additionally nucleate microtubules from the dendrite tip to organize dendritic microtubules. The relative contribution of these two mechanisms to organize microtubules in dendrites varies for different neurons. Whereas the URX dendrite microtubule organization is hardly affected by the *unc-33* mutation, suggesting that distal microtubule nucleation is dominant, the ASER dendrite does show some mixed microtubules in the proximal dendrite, suggesting that both mechanisms are important. These differences probably explain why we did not observe RAB-3 mislocalization in the URX neuron, whereas that was previously reported for other ciliated head neurons (Maniar et al., 2011). Moreover, although most ciliated neurons in *C. elegans* grow their dendrite by anchoring the tip/centriole and retracting their cell body (Heiman and Shaham, 2009; Schouteden et al., 2015), it was recently shown that the PQR neuron first extends its dendrite and then translocates its centrioles to the dendrite tip (Li et al., 2017), suggesting that both mechanisms are sequentially important. Interfering with both mechanisms (GIP-2 depletion in the *unc-33* or *unc-116* mutant) did not lead to a reversed microtubule polarity in the ciliated URX neuron, which might be expected. However, since the GIP-2 depletion is driven by a neuron-specific promoter so as to not interfere with cell division, the GIP-2 depletion is likely to be incomplete during early neuron development. The anchoring and nucleation of microtubules to the dendrite tip may be a valuable strategy to efficiently transport cargo to and from a distal sensory structure, such as the cilium. Indeed, when we inhibit microtubule nucleation, we affect the transport of RAB-8 and Golgi structures in the distal dendrite, and the targeting of GCY-35 to the URX sensory tip. This suggests that microtubule nucleation from the dendrite tip differentially organizes the distal microtubules to facilitate transport, either by generating more microtubule tracks and/or by generating a pool of more-dynamic tracks. The Taxol experiments would favor the former possibility; however, we did not observe an increased density of microtubules in the distal segment (Fig. 1A).

The basal body in dendritic tips can function as a microtubule organizer

The presence of a distal dendritic cilium is not specific to *C. elegans*; vertebrate olfactory neurons and photoreceptor cells also have specialized cilia structures at the tip of their dendrites (Louvi and Grove, 2011). In non-neuronal cells, it is well established that the basal body can function as a microtubule organizer (Moser et al., 2010), but in vertebrate neurons the centrosome (or basal body) is generally considered to lose its MTOC function during neuron maturation (Stiess et al., 2010). In frog olfactory neurons and teleost photoreceptor cells, however, microtubules have been found anchored to the basal body. Moreover, microtubules regrow from the basal body in photoreceptor cells after cold-induced microtubule depolymerization, suggesting that the basal body still functions as an MTOC (Burton, 1985; Reese, 1965; Troutt et al., 1990). Interestingly, in vertebrate olfactory neurons and photoreceptor cells, the microtubule polarity is uniformly minus-end out, as in *C. elegans* (Burton, 1985; Troutt and Burnside, 1988; Tsai et al., 2010). Therefore, vertebrate neurons may also employ distinct mechanisms to organize dendritic microtubule polarity; in most neurons, dendritic microtubules are organized with mixed polarity by a largely unknown mechanism, while in some specialized cells the basal body in the dendritic tip functions as an MTOC to organize microtubules.

Microtubule organization in non-ciliated neurons

For non-ciliated *C. elegans* neurons and for most vertebrate neurons, it is still unclear how dendrites acquire minus-end out microtubules. In this study, we compared several mutants that were reported to result in either mixed or reversed dendritic microtubule polarity (Goodwin et al., 2012; Maniar et al., 2011; Yan et al., 2013). Loss of *unc-44* (ankyrin), and to a lesser extent *unc-33* (CRMP), affects neuronal development and causes a mostly mixed microtubule polarity in both the axon and the dendrites, suggesting that the encoded proteins play a general role in neuronal microtubule organization. Since ankyrin proteins in mammalian neurons can anchor microtubules to the sub-membrane cytoskeleton (Freal et al., 2016), this might suggest that UNC-44 and UNC-33 have a similar structural role. On the other hand, *unc-116* (kinesin-1) shows a dose-dependent microtubule reversal phenotype, suggesting a different mode of action, potentially by mediating sliding of microtubules into the correct organization (Yan et al., 2013). Both *unc-33* and *unc-116* mutations lead to a reversal in dendritic microtubule polarity in the PVD dendrite, but have different effects in the PHC neuron, as reported previously (Maniar et al., 2011; Yan et al., 2013). Our results highlight the importance of examining individual neurons when studying gene loss-of-function phenotypes. Interestingly, in *Drosophila*, microtubule sliding mediated by kinesin-1 was shown to be important in dendrites as well as axons, where it uses an additional microtubule-binding domain in the tail to slide microtubules over other microtubules (Winding et al., 2016). In the absence of such microtubule–microtubule sliding, one might expect microtubules of mixed polarity to appear; however, this is not observed in the *C. elegans* *unc-116* mutant. In future studies, further examination of the relationship between *unc-33* and *unc-116* will help clarify how minus-end out microtubules are organized in non-ciliated neurons. It is interesting to note that both UNC-33 and UNC-116 can bind to the *C. elegans* kinesin light chain (KLC-2) (Tsuboi et al., 2005).

However, no microtubule polarity defects were reported for the hypomorphic *klc-2* mutant (Yan et al., 2013).

In summary, in this study, we found that *C. elegans* neurons employ distinct mechanisms to organize minus-end out microtubules in dendrites. We show that local microtubule nucleation from the dendrite tip generates an additional pool of microtubules, which can further fine tune the distal cargo transport. We suggest that mechanisms that regulate cargo transport by controlling local microtubule organization will also be used in more-complex animals.

MATERIALS AND METHODS

C. elegans strains and culturing

Strains were cultured using standard conditions at 15°C and imaged at room temperature. See Table S1 for an overview of all strains used.

The *unc-44(hrt2)* allele used in this study was made using CRISPR-mediated mutagenesis (Waaijers et al., 2013) generating a 111 bp deletion in the long exon (5′-ACGATAAGAAAACTATG…TATGAATCCGCCCA-AG-3′). For all strains crossed with MosSCI transgenes, the loss of the *unc-119(ed3)* injection marker was not confirmed (except for STR66 and STR71).

The *ceIs276[Punc17β::Cre]* strain was generated by means of CRISPR-based single-copy insertion in *unc-119(ed3)* at the targeted locus (position 3,561,295 on chromosome III; −5.5 m.u.), which we then followed by positive and negative selection methods (Dickinson et al., 2013; Frøkjaer-Jensen et al., 2012). Details of the generation of the *sup-1* minigene and floxed *unc-116(ce815)* allele can be found below.

To generate the *unc-116*-null mutant, we first crossed the floxed *unc-116* allele over the *hT2* balancer and expressed Cre in the germline by injecting the *Ppie-1::Cre* construct (Ruijtenberg and van den Heuvel, 2015). Homozygous *unc-116*-null mutants are growth arrested at approximately L2 stage, and thus were analyzed as young animals.

Expression constructs

Most constructs were generated by using multisite Gateway cloning (Invitrogen) and were sequenced for verification. Gateway 5′ entry clones were made by PCR amplifying upstream promoter sequences from genomic DNA and cloning into pDONRP4-P1R to generate entry clones; 2 kb for *Pmec-17* (Zheng et al., 2015), 4 kb for *Pceh-10* (Bertrand and Hobert, 2009), 3 kb for *Pgcy-5* (Yu et al., 1997), 2.4 kb for *Pida-1* (Yan et al., 2013). *Pdes-2* and *Pgcy-36* in pDONRP4-P1R were as described previously (Harterink et al., 2017, 2016). The middle entry clones were made by PCR amplifying the coding sequence of *tbg-1*, the N-terminus of aman-2 (amino acids 1–82; Edwards et al., 2013) from total cDNA, *ebp-2*, *gfp*, *ebp-2::gfp* and *mKate2* from plasmid DNA [*Pdes-2::ebp-2::gfp*, kind gift from Cori Bargmann (The Rockefeller University, USA) (Maniar et al., 2011)], and *mKate2* in pDONRP2R-P3 [gift from Henrik Bringmann (Max Planck Institute for Biophysical Chemistry, Germany); Redemann et al., 2011], which were cloned into pDONR221. 3′ entry clones were made by PCR amplifying the coding sequence of *rab-3*, *rab-8*, *maph-1* from total cDNA and cloning into pDONRP2R-P3. *gfp* (Addgene #21509, deposited by Julie Ahringer; Zeiser et al., 2011), *tbb-2* UTR (Addgene #17249, deposited by Geraldine Seydoux; Merritt et al., 2008) and *mKate2* were also used. Assembly LR reactions were performed using pCFJ150 for LGII, pCFJ210 for LGI (Frøkjaer-Jensen et al., 2012) or for LGIV pKN146, which is the pCFJ201 vector supplemented with the *unc-54* 3′ UTR (gift from Rik Korswagen, Hubrecht Institute, The Netherlands).

Pgcy-36::nls::tagBFP::p2A::GFPvhh::zif-1 and *Pgcy-36::gcy-35::mKate2* were cloned into the pCFJ350 backbone by performing Cold Fusion cloning (System Biosciences). We inserted mKate2 after the codon encoding S671 of *gcy-35* to generate a functional expression construct (Gross et al., 2014). The *Punc-17β::NLS-Cre::unc-54 UTR* insertion repair template was cloned, through a Gibson assembly reaction, so as to contain 1.5 kb genomic homology arms flanking and the *unc-119* marker gene (Frøkjaer-Jensen et al., 2008) in a pBS II plasmid background with the PAM site mutated. We inserted the protospacer sequence 5′-GATAAATCTGC-GCGTCAAGTATGG-3′ into the pDD162 Cas9-sgRNA plasmid by Q5 site-directed mutagenesis, as described for similar constructions (Dickinson et al., 2013).

Detailed subcloning information will be provided upon request.

The *sup-1* minigene – a small CRISPR marker designed for insertion in introns

To design a marker gene that could be expressed from an intron for CRISPR gene editing, we designed a marker around four guidelines: (1) that it be easily recognizable on culture plates when screening large populations of animals; (2) that it should be small, so as to not hinder the construction of large plasmid repair templates; (3) that is be relatively AT rich to mimic intronic sequence; and (4) that it should not contain splice acceptor sites in the reverse orientation. Therefore, we used the 103-amino-acid *sup-1(e995)* mutant gene that can dominantly rescue the strongly uncoordinated phenotype of *unc-17(e245)* (Mathews et al., 2012).

We designed a *sup-1* minigene that can be inserted in introns as a gene-editing marker (Fig. S4A); this contained a 491 bp *unc-17β* promoter to drive expression specifically in cholinergic motor neurons of the ventral nerve cord (AS, DA, DB, VA, VB neuron classes) followed by the *sup-1* gene carrying the *e995* suppressor mutation and the *C. briggsae unc-119* 3′ UTR (Frøkjaer-Jensen et al., 2008). After searching the reverse orientation of the minigene sequence with the consensus spice acceptor sequence WTNYAG, we replaced 11 potential splice acceptors in the coding region (silent mutations), intron and 3′ UTR. The total size of the *sup-1* minigene is 1112 bp, making it about half the size of *unc-119*, the next smallest marker gene used for gene editing in *C. elegans* (2129 bp).

sup-1(e995) minigene sequence was as follows [note that this is the reverse complement of the *sup-1(e995)* minigene sequence, and it should be directly inserted in the intron in this orientation]: CCTAGTTCTATACAT-TCTCTAATGAAAAAATCTTTCATTTGAAATTGAAAATGAGTTAA-AGTTGGAGTTTTTATTGAAAACAGATTTCCGTGTGATTAGTGTT-TTTAACGAGTGTGACAGGACAGCGAAAAAATATAAAAACAAGG-GGGGAACTGAAAAGCTTAGGAATGCATTGAACATGAGAAGGG-GAAGGGGAAGGAACAAACTAGACAGGAATTATTGGAATTTAAT-CACATTTGGAGTTTTTTTTCTATTCGACAGAATAATTATCCAAAA-CATTTTTGTATTAAATATCTACTTGCGGCAGCAGATGCAACGGA-CAAGGGAGATGACGAAGGAGGCGATGAAGATGACTTCGAACA-AGGCGAGGGTTACCCAGACCCATGTCTGGAGGTTAAAGCAGCA-TTCCTTGTTGAGTTCTCCACAGCATTTCCAATAGTGGAAGATGC-TAGAGGTTCCGCATTTGGTTCCGACCAATGGTACCGGGCAATAT-GTGTCTCCGTCCTGAAAATTTTTAAAAATTTTGAAGATATATAA-GAGGAAAAGTACCTTTGTGGTGGTGACCTCATTCACTGCACTTT-TCACGTCGTGGTCCACGTTGGCAGCCATTGCGAGTCCAATGCAC-GCGGCGAGTGCGATGTAAGACATCATTTTGATAGGTTAAGCTG-AAAATTAAATATTTTATTGTAAAACTTTTGGGGGCAAAATAAAA-AAATAAAGAGGAAACAAGGAACTTGAAAAATAAAATAAAAAT-TATTTTTTTGAAAAATTCCGGCGGGAAAATTATTTTTTGACAAA-AAAAAAGAATTTTTTCTGAAATTTTAGTTTAAAAAGTTCAAATG-ACTCCACCGAGTTACCTTAAAAAATTGCTAAACACTAATTTAGG-CTAAAAATCAGGCGAAAAAAGAAAAATGACATGTGTATTTGAG-CCCCCGGGCGGGTTTCTTTTCTGTTCTGAGGGATGACTCTATTG-TTATTTTTTACGAAGATTGCCTTGGTGTATAAATGTACAGCTCCC-CGGGGACCATTCCAATATCTTCTCTCCCAACTTTCTCCTCTCAAA-ATTCCCGCAAAAATCCCAAAAACCAGAAAATTGTGAAAACCAA-AAGCTT.

Floxing the *unc-116* (kinesin-1) gene

To target the necessary modifications to the *unc-116* gene, we made a plasmid template in which we inserted the *sup-1* minigene in reverse orientation in the 168 bp intron 2, and LoxP sites in the 5′ UTR and intron 4 (Fig. S4B). Excision of the sequences between the LoxP sites would remove most of the motor domain of the kinesin. We flanked the modifications with 1500-bp homology arms. Our single guide (sg)RNA targeted a cut site between the first LoxP site and the *sup-1* minigene insertion (Fig. S4B). These modifications were distributed such that there was 235 and 847 bp of unmodified genomic sequences between the LoxP sites and the *sup-1* minigene.

To target the template to the desired genomic location, we again used the method of Dickinson et al. (Dickinson et al., 2013), except that we injected

unc-17(e245) mutants and screened for *sup-1*-mediated rescue of the Unc phenotype of the mutant. We injected 174 animals, plated them at three per plate, and recovered two lines of *sup-1* rescued animals that survived the PEEL-1-negative selection. We were unable to make one of the lines homozygous, suggesting that an error in the homologous recombination process had damaged the *unc-116* gene. PCR analysis with flanking primers revealed that the second line contained a modified template of the expected size at the expected location; however, sequencing revealed that it was missing the first LoxP site. We therefore used oligo-templated co-conversion (Arribere et al., 2014) to insert this LoxP site and designated the new mutant *unc-116(ce815)*. This strain appeared indistinguishable from wild type with respect to growth, fertility and egg laying, indicating that the intron-inserted *sup-1* minigene was not disrupting gene function. We confirmed that the single-copy Cre insertion excised the LoxP sites in the *unc-116* gene by crossing the Cre insertion *ceIs276[Punc-17β::Cre]* with the floxed *unc-116* gene and amplifying genomic DNA using primers flanking the LoxP sites (results not shown).

Imaging and data analysis

All live imaging was performed on a Nikon Eclipse-Ti microscope with a Plan Apo VC, 60×, 1.40 NA oil (Nikon) or a Plan Apo VC 100× N.A. 1.40 oil objectives, or, for laser-induced severing experiments, an S Fluor 100×, 0.5–1.3 NA oil-immersion objective (Nikon). The microscope is equipped with a motorized stage (ASI; PZ-2000), a Perfect Focus System (Nikon), the ILas system (Roper Scientific France/PICT-IBiSA, Curie Institute) and uses MetaMorph 7.8.0.0 software (Molecular Devices) to control the camera and all motorized parts. Confocal excitation and detection is achieved using 100 mW Cobolt Calypso 491 nm and 100 mW Cobolt Jive 561 nm lasers, and a Yokogawa spinning disc confocal scanning unit (CSU-X1-A1N-E; Roper Scientific) equipped with a triple-band dichroic mirror (z405/488/568trans-pc; Chroma) and a filter wheel (CSUX1-FW-06P-01; Roper Scientific) containing GFP [ET-GFP (49002)] and mCherry [ET-mCherry (49008)] emission filters (all Chroma). A Teem Photonics 355 nm Q-switched pulsed laser was used for laser severing (Yau et al., 2016). Confocal images were acquired with a QuantEM:512 SCEMCCD camera (Photometrics) at a final magnification of 110 nm (60× objective) or 67 nm (100× objective) per pixel, including the additional 2.0× magnification introduced by an additional lens mounted between scanning unit and camera (Edmund Optics).

All other images, except for those shown in Fig. S1B, were acquired using a LSM700 (Zeiss) microscope with a 63×/1.40 oil or 40×/1.30 oil DIC objective using 405 nm, 488 nm and 555 nm laser lines. Images in Fig. S1B, were taken on an Olympus BX53 fluorescence microscope, with a UPLFLN 40×O/1.3 oil objective and Photometrics CoolSNAP HQ2 CCD camera.

For imaging, L4 or young adult worms were anesthetized with 10 mM tetramisole on a 5% agarose pad and all live imaging was performed within 60 min. Especially for the imaging of EBP-2 dynamics, we noticed that pre-incubating the agarose pad in M9 buffer resulted in significantly better preservation of the microtubule dynamics. All EBP-2::GFP imaging was performed at 1 frame per s (fps) (or 2 fps for laser-severing experiments); when necessary, *z*-stacks were taken with a 1 µm step size and maximum intensity projections and further processing was performed using ImageJ software (NIH).

For the quantifications of microtubule growth speeds, only growth events of >2 µm were considered. For the quantification of growth distance and catastrophe frequencies, only growth events entirely inside the kymograph were used (minimum of 20 pixels from the sides and 10 pixels from the top/bottom; at 100×1 µm=15.1 pixels). In the *unc-44* mutant (and to lesser extent also in the *unc-33* and *unc-116* mutants) neuron development is compromised; neurons with ectopic branches from the cell body or other considerable developmental defects were not imaged. Furthermore, the extrachromosomal EBP-2::GFP lines have variable expression, sometimes resulting in static puncta or vesicular-like dynamics (moving up and down the neurite), which were not used for quantifications. The AVA neuron was imaged in the proximal region next to the pharynx before it reaches the ventral nerve cord.

The RAB-8 and AMAN-2 dynamics were imaged at 2 fps. For the RAB-8 kymographs, the average movie intensity was subtracted from the movie before making the kymographs. RAB-8 dynamics were quantified by counting the average number of cargo crossings at three positions in the either the proximal or distal dendrite for each kymograph.

For Taxol-induced microtubule stabilization, we pre-incubated the worms within M9 buffer containing 10 µM tetramisole together with 10 µM Taxol (including 1% DMSO) or 1% DMSO, as a control, for 40 min in an Eppendorf tube, before mounting on an agarose pad.

To quantify GIP-2::GFP levels at the dendrite tip, we made confocal stacks (0.57 µm step size) and used ImageJ to make a sum projection of three frames around the dendrite tip of mid-dendrite region. The mean intensity of each region was measured in a 10-pixel round selection.

Images and movies were rotated and if necessary flipped to have the anterior to the left and ventral side down. All statistics were determined by using GraphPad.

Acknowledgements

We thank C. Bargmann, H Bringmann, R. Korswagen, M. Galli, F. Horndli and V. Portegijs for constructs; K. Shen for the *wyEx4828* and *wySi265;wyIs364* strains (Yan et al., 2013); F. McNally for the *unc-116(rh24sb79)* strain (Yang et al., 2005); K. Oegema for the *gip-2* gfp knock-in strain and epiDEG construct (Wang et al., 2015); the *Caenorhabditis* Genetics Center, which is funded by the NIH Office of Research Infrastructure Programs (P40 OD010440) for strains, Brenda Szymkiewicz for technical assistance; and WormBase.

Competing interests

The authors declare no competing or financial interests.

Author contributions

Conceptualization: M.H., S.L.E., K.W.Y., S.v.d.H., L.C.K., K.M., C.C.H.; Methodology: M.H., S.L.E., C.C.H.; Formal analysis: M.H.; Investigation: M.H., S.L.E., B.d.H., K.W.Y.; Resources: M.H., S.L.E., B.d.H.; Writing - original draft: M.H., S.L.E., K.M., C.C.H.; Writing - review & editing: M.H., S.v.d.H., L.C.K., K.M., C.C.H.; Visualization: M.H., S.L.E., K.M.; Supervision: M.H., S.v.d.H., K.M., C.C.H.; Project administration: M.H., C.C.H.; Funding acquisition: M.H., K.M., C.C.H.

Funding

This work is supported by the Nederlandse Organisatie voor Wetenschappelijk Onderzoek (NWO) (NWO-ALW-VENI 863.12.001 to M.H., NWO-ALW-VIDI 864.12.008 to L.C.K., NWO-ALW-VICI 865.10.010 to C.C.H.) by the European Research Council (ERC Starting Grant 336291 to L.C.K., ERC Consolidator Grant 617050 to C.C.H.) and by a grant from the National Institute of General Medical Sciences of the National Institutes of Health (R01GM080765 to K.G.M.). Deposited in PMC for release after 12 months.

Supplementary information

Supplementary information available online at
http://jcs.biologists.org/lookup/doi/10.1242/jcs.223107.supplemental

References

Arribere, J. A., Bell, R. T., Fu, B. X. H., Artiles, K. L., Hartman, P. S. and Fire, A. Z. (2014). Efficient marker-free recovery of custom genetic modifications with CRISPR/Cas9 in Caenorhabditis elegans. *Genetics* **198**, 837-846.

Baas, P. W. and Lin, S. (2011). Hooks and comets: The story of microtubule polarity orientation in the neuron. *Dev. Neurobiol.* **71**, 403-418.

Baas, P. W., Deitch, J. S., Black, M. M. and Banker, G. A. (1988). Polarity orientation of microtubules in hippocampal neurons: uniformity in the axon and nonuniformity in the dendrite. *Proc. Natl. Acad. Sci. USA* **85**, 8335-8339.

Bertrand, V. and Hobert, O. (2009). Linking asymmetric cell division to the terminal differentiation program of postmitotic neurons in C. elegans. *Dev. Cell* **16**, 563-575.

Bobinnec, Y., Fukuda, M. and Nishida, E. (2000). Identification and characterization of Caenorhabditis elegans gamma-tubulin in dividing cells and differentiated tissues. *J. Cell Sci.* **113**, 3747-3759.

Bounoutas, A. and Chalfie, M. (2007). Touch sensitivity in Caenorhabditis elegans. *Pflugers Arch.* **454**, 691-702.

Burton, P. R. (1985). Ultrastructure of the olfactory neuron of the bullfrog: the dendrite and its microtubules. *J. Comp. Neurol.* **242**, 147-160.

Cheung, B. H., Arellano-Carbajal, F., Rybicki, I. and de Bono, M. (2004). Soluble guanylate cyclases act in neurons exposed to the body fluid to promote C. elegans aggregation behavior. *Curr. Biol.* **14**, 1105-1111.

del Castillo, U., Winding, M., Lu, W. and Gelfand, V. I. (2015). Interplay between kinesin-1 and cortical dynein during axonal outgrowth and microtubule organization in Drosophila neurons. *Elife* **4**, e10140.

Dickinson, D. J., Ward, J. D., Reiner, D. J. and Goldstein, B. (2013). Engineering the Caenorhabditis elegans genome using Cas9-triggered homologous recombination. *Nat. Methods* **10**, 1028-1034.
Doroquez, D. B., Berciu, C., Anderson, J. R., Sengupta, P. and Nicastro, D. (2014). A high-resolution morphological and ultrastructural map of anterior sensory cilia and glia in Caenorhabditis elegans. *Elife* **3**, e01948.
Edwards, S. L., Yu, S.-C., Hoover, C. M., Phillips, B. C., Richmond, J. E. and Miller, K. G. (2013). An organelle gatekeeper function for Caenorhabditis elegans UNC-16 (JIP3) at the axon initial segment. *Genetics* **194**, 143-161.
Freal, A., Fassier, C., Le Bras, B., Bullier, E., De Gois, S., Hazan, J., Hoogenraad, C. C. and Couraud, F. (2016). Cooperative interactions between 480 kDa Ankyrin-G and EB proteins assemble the axon initial segment. *J. Neurosci.* **36**, 4421-4433.
Frøkjaer-Jensen, C., Davis, M. W., Hopkins, C. E., Newman, B. J., Thummel, J. M., Olesen, S. P., Grunnet, M. and Jorgensen, E. M. (2008). Single-copy insertion of transgenes in Caenorhabditis elegans. *Nat. Genet.* **40**, 1375-1383.
Frøkjaer-Jensen, C., Davis, M. W., Ailion, M. and Jorgensen, E. M. (2012). Improved Mos1-mediated transgenesis in C. elegans. *Nat. Methods* **9**, 117-118.
Goodwin, P. R., Sasaki, J. M. and Juo, P. (2012). Cyclin-dependent kinase 5 regulates the polarized trafficking of neuropeptide-containing dense-core vesicles in Caenorhabditis elegans motor neurons. *J. Neurosci.* **32**, 8158-8172.
Gross, E., Soltesz, Z., Oda, S., Zelmanovich, V., Abergel, Z. and de Bono, M. (2014). GLOBIN-5-dependent O2 responses are regulated by PDL-1/PrBP that targets prenylated soluble guanylate cyclases to dendritic endings. *J. Neurosci.* **34**, 16726-16738.
Harterink, M., van Bergeijk, P., Allier, C., de Haan, B., van den Heuvel, S., Hoogenraad, C. C. and Kapitein, L. C. (2016). Light-controlled intracellular transport in Caenorhabditis elegans. *Curr. Biol.* **26**, R153-R154.
Harterink, M., da Silva, M. E., Will, L., Turan, J., Ibrahim, A., Lang, A. E., van Battum, E. Y., Pasterkamp, R. J., Kapitein, L. C., Kudryashov, D. et al. (2017). DeActs: genetically encoded tools for perturbing the actin cytoskeleton in single cells. *Nat. Methods* **14**, 479-482.
Heiman, M. G. and Shaham, S. (2009). DEX-1 and DYF-7 establish sensory dendrite length by anchoring dendritic tips during cell migration. *Cell* **137**, 344-355.
Kapitein, L. C. and Hoogenraad, C. C. (2015). Building the neuronal microtubule Cytoskeleton. *Neuron* **87**, 492-506.
Kaplan, O. I., Molla-Herman, A., Cevik, S., Ghossoub, R., Kida, K., Kimura, Y., Jenkins, P., Martens, J. R., Setou, M., Benmerah, A. et al. (2010). The AP-1 clathrin adaptor facilitates cilium formation and functions with RAB-8 in C. elegans ciliary membrane transport. *J. Cell Sci.* **123**, 3966-3977.
Kurup, N., Yan, D., Goncharov, A. and Jin, Y. (2015). Dynamic microtubules drive circuit rewiring in the absence of neurite remodeling. *Curr. Biol.* **25**, 1594-1605.
Li, W., Yi, P., Zhu, Z., Zhang, X., Li, W. and Ou, G. (2017). Centriole translocation and degeneration during ciliogenesis in Caenorhabditis elegans neurons. *EMBO J.* **123**, 3966-3977.
Louvi, A. and Grove, E. A. (2011). Cilia in the CNS: the quiet organelle claims center stage. *Neuron* **69**, 1046-1060.
Maniar, T. A., Kaplan, M., Wang, G. J., Shen, K., Wei, L., Shaw, J. E., Koushika, S. P. and Bargmann, C. I. (2011). UNC-33 (CRMP) and ankyrin organize microtubules and localize kinesin to polarize axon-dendrite sorting. *Nat. Neurosci.* **15**, 48-56.
Mathews, E. A., Mullen, G. P., Hodgkin, J., Duerr, J. S. and Rand, J. B. (2012). Genetic interactions between UNC-17/VAChT and a novel transmembrane protein in Caenorhabditis elegans. *Genetics* **192**, 1315-1325.
Merritt, C., Rasoloson, D., Ko, D. and Seydoux, G. (2008). 3′ UTRs are the primary regulators of gene expression in the C. elegans germline. *Curr. Biol.* **18**, 1476-1482.
Modzelewska, K., Lauritzen, A., Hasenoeder, S., Brown, L., Georgiou, J. and Moghal, N. (2013). Neurons refine the Caenorhabditis elegans body plan by directing axial patterning by Wnts. *PLoS Biol.* **11**, e1001465.
Moser, J. J., Fritzler, M. J., Ou, Y. and Rattner, J. B. (2010). The PCM-basal body/primary cilium coalition. *Semin. Cell Dev. Biol.* **21**, 148-155.
Moughamian, A. J., Osborn, G. E., Lazarus, J. E., Maday, S. and Holzbaur, E. L. F. (2013). Ordered recruitment of dynactin to the microtubule plus-end is required for efficient initiation of retrograde axonal transport. *J. Neurosci.* **33**, 13190-13203.
Nechipurenko, I. V., Berciu, C., Sengupta, P. and Nicastro, D. (2017). Centriolar remodeling underlies basal body maturation during ciliogenesis in Caenorhabditis elegans. *Elife* **6**, e25686.
Rao, A. N., Patil, A., Black, M. M., Craig, E. M., Myers, K. A., Yeung, H. T. and Baas, P. W. (2017). Cytoplasmic dynein transports axonal microtubules in a polarity-sorting manner. *Cell Rep* **19**, 2210-2219.
Rawson, R. L., Yam, L., Weimer, R. M., Bend, E. G., Hartwieg, E., Horvitz, H. R., Clark, S. G. and Jorgensen, E. M. (2014). Axons degenerate in the absence of mitochondria in C. *elegans*. *Curr. Biol.* **24**, 760-765.
Redemann, S., Schloissnig, S., Ernst, S., Pozniakowsky, A., Ayloo, S., Hyman, A. A. and Bringmann, H. (2011). Codon adaptation-based control of protein expression in C. elegans. *Nat. Methods* **8**, 250-252.
Reese, T. S. (1965). Olfactory cilia in the frog. *J. Cell Biol.* **25**, 209-230.
Rolls, M. M. and Jegla, T. J. (2015). Neuronal polarity: an evolutionary perspective. *J. Exp. Biol.* **218**, 572-580.
Ruijtenberg, S. and van den Heuvel, S. (2015). G1/S Inhibitors and the SWI/SNF complex control cell-cycle exit during muscle differentiation. *Cell* **162**, 300-313.
Sanchez-Huertas, C., Freixo, F., Viais, R., Lacasa, C., Soriano, E. and Luders, J. (2016). Non-centrosomal nucleation mediated by augmin organizes microtubules in post-mitotic neurons and controls axonal microtubule polarity. *Nat. Commun.* **7**, 12187.
Schouteden, C., Serwas, D., Palfy, M. and Dammermann, A. (2015). The ciliary transition zone functions in cell adhesion but is dispensable for axoneme assembly in C. elegans. *J. Cell Biol.* **210**, 35-44.
Serwas, D., Su, T. Y., Roessler, M., Wang, S. and Dammermann, A. (2017). Centrioles initiate cilia assembly but are dispensable for maturation and maintenance in C. elegans. *J. Cell Biol.* **216**, 1659-1671.
Stepanova, T., Slemmer, J., Hoogenraad, C. C., Lansbergen, G., Dortland, B., De Zeeuw, C. I., Grosveld, F., van Cappellen, G., Akhmanova, A. and Galjart, N. (2003). Visualization of microtubule growth in cultured neurons via the use of EB3-GFP (end-binding protein 3-green fluorescent protein). *J. Neurosci.* **23**, 2655-2664.
Stiess, M., Maghelli, N., Kapitein, L. C., Gomis-Ruth, S., Wilsch-Brauninger, M., Hoogenraad, C. C., Tolic-Norrelykke, I. M. and Bradke, F. (2010). Axon extension occurs independently of centrosomal microtubule nucleation. *Science* **327**, 704-707.
Tas, R. P., Chazeau, A., Cloin, B. M. C., Lambers, M. L. A., Hoogenraad, C. C. and Kapitein, L. C. (2017). Differentiation between oppositely oriented microtubules controls polarized neuronal transport. *Neuron* **96**, 1264-1271 e5.
Taylor, C. A., Yan, J., Howell, A. S., Dong, X. and Shen, K. (2015). RAB-10 regulates dendritic branching by balancing dendritic transport. *PLoS Genet.* **11**, e1005695.
Troutt, L. L. and Burnside, B. (1988). Microtubule polarity and distribution in teleost photoreceptors. *J. Neurosci.* **8**, 2371-2380.
Troutt, L. L., Wang, E., Pagh-Roehl, K. and Burnside, B. (1990). Microtubule nucleation and organization in teleost photoreceptors: microtubule recovery after elimination by cold. *J. Neurocytol.* **19**, 213-223.
Tsai, J.-W., Lian, W.-N., Kemal, S., Kriegstein, A. R. and Vallee, R. B. (2010). Kinesin 3 and cytoplasmic dynein mediate interkinetic nuclear migration in neural stem cells. *Nat. Neurosci.* **13**, 1463-1471.
Tsuboi, D., Hikita, T., Qadota, H., Amano, M. and Kaibuchi, K. (2005). Regulatory machinery of UNC-33 Ce-CRMP localization in neurites during neuronal development in Caenorhabditis elegans. *J. Neurochem.* **95**, 1629-1641.
van Beuningen, S. F., Will, L., Harterink, M., Chazeau, A., van Battum, E. Y., Frias, C. P., Franker, M. A., Katrukha, E. A., Stucchi, R., Vocking, K. et al. (2015). TRIM46 controls neuronal polarity and axon specification by driving the formation of parallel microtubule arrays. *Neuron* **88**, 1208-1226.
Waaijers, S., Portegijs, V., Kerver, J., Lemmens, B. B. L. G., Tijsterman, M., van den Heuvel, S. and Boxem, M. (2013). CRISPR/Cas9-targeted mutagenesis in Caenorhabditis elegans. *Genetics* **195**, 1187-1191.
Wang, S., Wu, D., Quintin, S., Green, R. A., Cheerambathur, D. K., Ochoa, S. D., Desai, A. and Oegema, K. (2015). NOCA-1 functions with gamma-tubulin and in parallel to Patronin to assemble non-centrosomal microtubule arrays in C. elegans. *Elife* **4**, e08649.
Winding, M., Kelliher, M. T., Lu, W., Wildonger, J. and Gelfand, V. I. (2016). Role of kinesin-1-based microtubule sliding in Drosophila nervous system development. *Proc. Natl. Acad. Sci. USA* **113**, E4985-E4994.
Yan, J., Chao, D. L., Toba, S., Koyasako, K., Yasunaga, T., Hirotsune, S. and Shen, K. (2013). Kinesin-1 regulates dendrite microtubule polarity in Caenorhabditis elegans. *Elife* **2**, e00133.
Yang, H.-Y., Mains, P. E. and McNally, F. J. (2005). Kinesin-1 mediates translocation of the meiotic spindle to the oocyte cortex through KCA-1, a novel cargo adapter. *J. Cell Biol.* **169**, 447-457.
Yau, K. W., Schatzle, P., Tortosa, E., Pages, S., Holtmaat, A., Kapitein, L. C. and Hoogenraad, C. C. (2016). Dendrites in vitro and in vivo contain microtubules of opposite polarity and axon formation correlates with uniform plus-end-out microtubule orientation. *J. Neurosci.* **36**, 1071-1085.
Yogev, S., Cooper, R., Fetter, R., Horowitz, M. and Shen, K. (2016). Microtubule organization determines axonal transport dynamics. *Neuron* **92**, 449-460.
Yogev, S., Maeder, C. I., Cooper, R., Horowitz, M., Hendricks, A. G. and Shen, K. (2017). Local inhibition of microtubule dynamics by dynein is required for neuronal cargo distribution. *Nat. Commun.* **8**, 15063.
Yu, S., Avery, L., Baude, E. and Garbers, D. L. (1997). Guanylyl cyclase expression in specific sensory neurons: a new family of chemosensory receptors. *Proc. Natl. Acad. Sci. USA* **94**, 3384-3387.
Zeiser, E., Frokjaer-Jensen, C., Jorgensen, E. and Ahringer, J. (2011). MosSCI and gateway compatible plasmid toolkit for constitutive and inducible expression of transgenes in the C. elegans germline. *PLoS ONE* **6**, e20082.
Zheng, Y., Wildonger, J., Ye, B., Zhang, Y., Kita, A., Younger, S. H., Zimmerman, S., Jan, L. Y. and Jan, Y. N. (2008). Dynein is required for polarized dendritic transport and uniform microtubule orientation in axons. *Nat. Cell Biol.* **10**, 1172-1180.
Zheng, C., Diaz-Cuadros, M. and Chalfie, M. (2015). Hox genes promote neuronal subtype diversification through posterior induction in Caenorhabditis elegans. *Neuron* **88**, 514-527.